

## Accepted Manuscript

A Novel Multilayer Sandwich Fabric-based Composite Material for Infrared Stealth and Super Thermal Insulation Protection

Rui Xu, Wei Wang, Dan Yu

PII: S0263-8223(18)33997-7

DOI: <https://doi.org/10.1016/j.compstruct.2019.01.032>

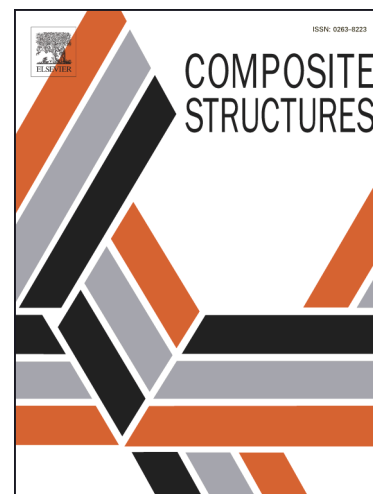
Reference: COST 10549

To appear in: *Composite Structures*

Received Date: 4 November 2018

Revised Date: 17 December 2018

Accepted Date: 3 January 2019



Please cite this article as: Xu, R., Wang, W., Yu, D., A Novel Multilayer Sandwich Fabric-based Composite Material for Infrared Stealth and Super Thermal Insulation Protection, *Composite Structures* (2019), doi: <https://doi.org/10.1016/j.compstruct.2019.01.032>

This is a PDF file of an unedited manuscript that has been accepted for publication. As a service to our customers we are providing this early version of the manuscript. The manuscript will undergo copyediting, typesetting, and review of the resulting proof before it is published in its final form. Please note that during the production process errors may be discovered which could affect the content, and all legal disclaimers that apply to the journal pertain.

# A Novel Multilayer Sandwich Fabric-based Composite Material for Infrared Stealth and Super Thermal Insulation Protection

Rui Xu<sup>a</sup>, Wei Wang<sup>a</sup>, Dan Yu<sup>a,\*</sup>

<sup>a</sup>Key Lab of Science & Technology of Eco-Textile, Ministry of Education, College of Chemistry, Chemical Engineering and Biotechnology, Donghua University, Shanghai 201620, China

\*Telephone: 86-21-67792456, Fax number: 86-21-67792608, E-mail: yudan@dhu.edu.cn.

## Abstract

At present, infrared stealth materials for advanced detection and stealth technology is usually prepared with low emissivity coating on the surface, but there are very few efficient infrared stealth materials based on textiles with lightweight and flexible features. In this paper, we designed a carbon nanotube-doped aerogel (CNTAs) sandwich structure on polyimide (PI) fabric by hot pressing and then coated with a low emissivity Al-doped ZnO (ZAO) on the outer surface. The surface emissivity lower than 0.5 due to the existence of ZAO and the thermal conductivity of the intermediate interlayer aerogels as low as 0.013 W/(m•K). Additionally, through experiments, theoretical derivation and simulation analysis, we found the resultant composite demonstrated a high infrared stealth performance with super insulation effect, implying it will have a fine prospect in infrared stealth and thermal insulation protection fields with its unique structure and excellent properties.

**Keywords:** Infrared Stealth; Thermal Insulation; Carbon Nanotube-doped Aerogel; Al-doped ZnO; Sandwich Structure; Polyimide Fabric.

## 1 Introduction

With the rapid development of infrared (IR) detection systems and the improvement of detection accuracy, the security and survival of military equipment and facilities have been seriously threatened [1-3]. Therefore, IR stealth provides a guarantee for the survival of soldiers and weapons, and plays an extremely important role in the battlefield [4, 5]. However, all objects above absolute zero will emit IR radiation [6], and IR detection just relies on the difference in IR radiation between the target and the background to detect the target [1]. Needless to say, soldiers and weapons often have higher temperatures than their environment, especially at night, as they will exhibit high brightness on an infrared thermal imaging in contrast with the background[6]. According to Stefan-Boltzmann's law[7], there are two main methods to reduce the infrared radiation of the target: one is to reduce the emissivity of the target surface; the other is to control the temperature of the target surface. Therefore, take these two factors into account; the key to stealth technique is to prepare a functional composite with isolate heat structure inside combining with low surface emissivity outside.

This functional composite can not only used in infrared stealth fields, but also in high-temperature environments such as steelmaking, ironmaking, and firefighting when based on textiles as it has a good heat isolation function with flexible and lightweight features[8]. This composite can also be used in the energy-saving fields like building upholstery [8, 9]. Therefore, the development of infrared stealth material based on textiles with excellent thermal insulation properties is great significance, while fire retardancy, resilience and flexibility are also demanded in practical use [8, 10].

Typical insulation materials, including wool, Styrofoam, and cork, usually exhibit near air thermal conductivity ( $0.03 \text{ W}/(\text{m}\cdot\text{K})$ ), which is essentially isotropic and not ideal for effective thermal management [11]. It is reported that the thermal conductivity of the insulating material prepared by silica aerogel is very low, which is about  $0.013 \text{ W}/(\text{m}\cdot\text{K})$  [8, 12]. In addition to good thermal insulation properties, the

Al-doped ZnO (ZAO) has an infrared emissivity as low as 0.5. This is because ZnO is a kind of semiconductor filler, but due to the gap of ZnO itself, the vacancies of  $\text{Zn}^{2+}$  and oxygen result in higher resistivity and narrow band gap, therefore pure ZnO has weak infrared stealth performance [13]. When doped with the aluminum element can increase the free carrier concentration, so that the infrared light region is strongly absorbed and reflected, and the electrical conductivity and optical properties are improved [14]. Furthermore, ZAO has high reflectivity in the infrared band (about 1,000-10,000 nm). It can reflect a large amount of thermal radiation energy when applied to coatings. For example, Li Gong et al.[15] prepared a ZAO film by pulsed laser deposition with low transmittance (<15% at 1,500 nm) and high reflectance (<50% at 2,000 nm) in the near-infrared region.

The form of fillers and the structure of composite materials are both vital to the thermal insulating effect. For example, Faheem Ahmad et al. [16] synthesized a novel composite of aerogel with polyester nonwoven fabric by a sol-gel method. The thermal diffusivity of the composite of aerogel was significantly lower than that of the pure polyester nonwoven material. Chang-Yeoul Kim et al. [17] prepared the glass fiber doped aerogels composite by using glass fiber as reinforcing phase through surface modification. However, as a material with the high porosity and porous network structure, aerogel prone to break easily and even collapse, how to improve its mechanical properties is still a challenge. Aiming this, we choose carbon nanotubes (CNTs), which has the highest elastic modulus of known materials and their diameters are about several nanometers to dozens of nanometers, which is equivalent to the aerogel microstructure size, so they can be used to enhance the mechanical properties of aerogels. At present, the preparation of infrared stealth materials is usually coated with metal particles on the surface, and there are few high-efficiency and lightweight infrared stealth materials based on textiles [18]. To our knowledge, there are no reports on the design of structures with super thermal insulation inside joined with low surface emissivity outside. In addition, the relation of infrared stealth performance with the structured design is not fully understood by previous literatures. Hence, we proposed to investigate the mechanism by theoretical derivations and

simulations.

In this paper, a carbon nanotube-doped aerogel (CNTAs) with sandwich structure was hot pressed on polyimide (PI) fabric, and then coated a low emissivity Al-doped ZnO (ZAO) on the outer surface. The preparing process of multilayer sandwich fabric-based composite material (ZAO/CNTAs/PI fabric) was illustrated in Fig. 1. The composites we prepared have high infrared stealth performance, super thermal insulation effects and excellent flame-retardant properties. We believe it will make them useful in many fields.

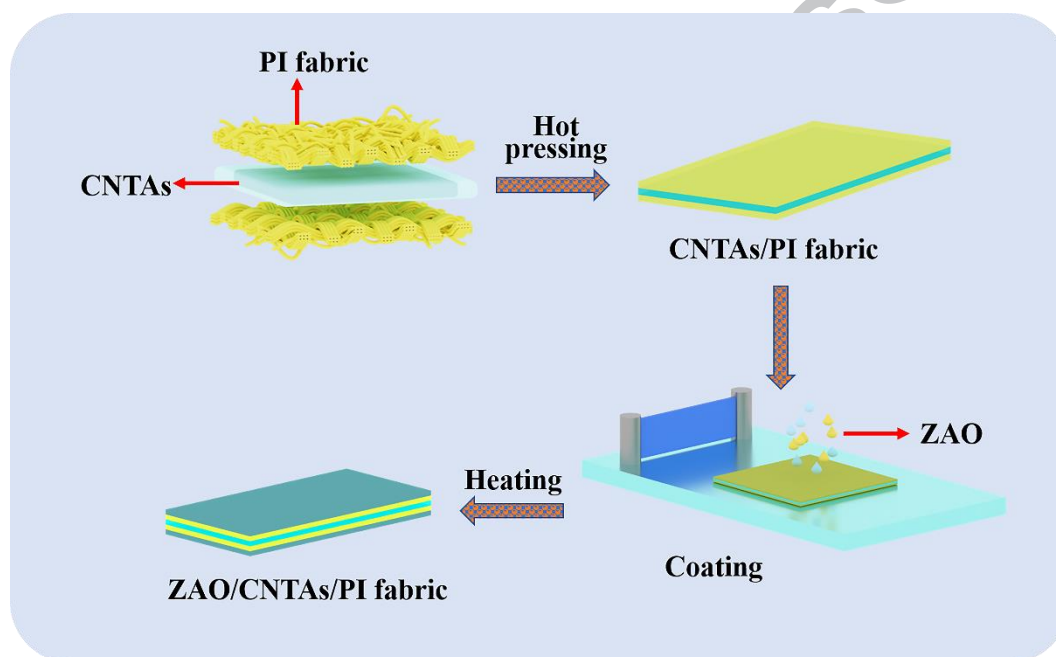


**Fig. 1** The process of the preparation of multilayer sandwich fabric-based composite material (ZAO/CNTAs/PI fabric).

## 2 Experimental section

### 2.1 Materials

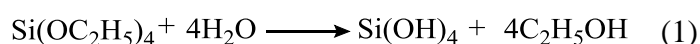
In the study, the PI fabric is purchased from Jiangsu Aoshen Hi-tech Materials Co. Carbon nanotubes (CNTs) were purchased from Sinopharm Chemical Reagent Co., Ltd. Ethylsilicate (TEOS) purchased from Shanghai Maclean Biochemical Technology Co., Ltd. Hydrochloric acid and ammonia water purchased from Shanghai Ling Feng chemical reagents Co., Ltd., diffusing agent purchased from Deqian (Shanghai, China) Chemical Co., Ltd., anhydrous alcohol purchased from Shanghai and Chemical Co., Ltd., thickener CN-WW purchased from Guangzhou

Cheng Na Chemical Co., Ltd., Zinc nitrate, aluminum nitrate, resin binder and polyethylene glycol-1540 were purchased from Sinopharm Chemical Reagent Co., Ltd. (Shanghai, China) without further purification, and the polyethylene glycol 1540 was chemical pure. The rest of the drugs were all analytically pure and no further purification were needed in the use process. All chemicals were analytic grade reagents and used without further purification.

## 2.2 Preparation of carbon nanotube aerogel

Ethylsilicate (TEOS), ethanol and deionized water were mixed at a molar ratio of 1:5:4 and stirred uniformly. Dilute hydrochloric acid was used to adjust the pH value of the solution to 3~4, stirring 30min, and let stand for 24 h. After the hydrolysis reaction was sufficient, an appropriate amount of dilute ammonia water was slowly added to adjust the pH to 6~7. At the same time, a small amount of carbon nanotubes was added to the solution. After stirring for 10 min, it was poured into a plastic container and allowed to stand and sealed until the sol was converted into a SiO<sub>2</sub> alcohol gel.

In order to further enhance the network skeleton structure, the alcohol gel was immersed in ethanol solution containing tetraethyl silicate for aging. After aging, the gel was replaced by a solvent with a lower surface tension. Then the hydroxyl alkylation on the surface of the gel was carried out with a surface modifier. Subsequently, n-hexane was replaced to remove the modified reactants and moisture remaining in the gel. Finally, the wet gel was dried at atmospheric pressure for 12 hours, and then the hydrophobic carbon nanotube aerogels were obtained. The process of the preparation of CNTAs was depicted in Fig. 2. The aerogel was prepared as following reaction (1)-(3) [19, 20]:



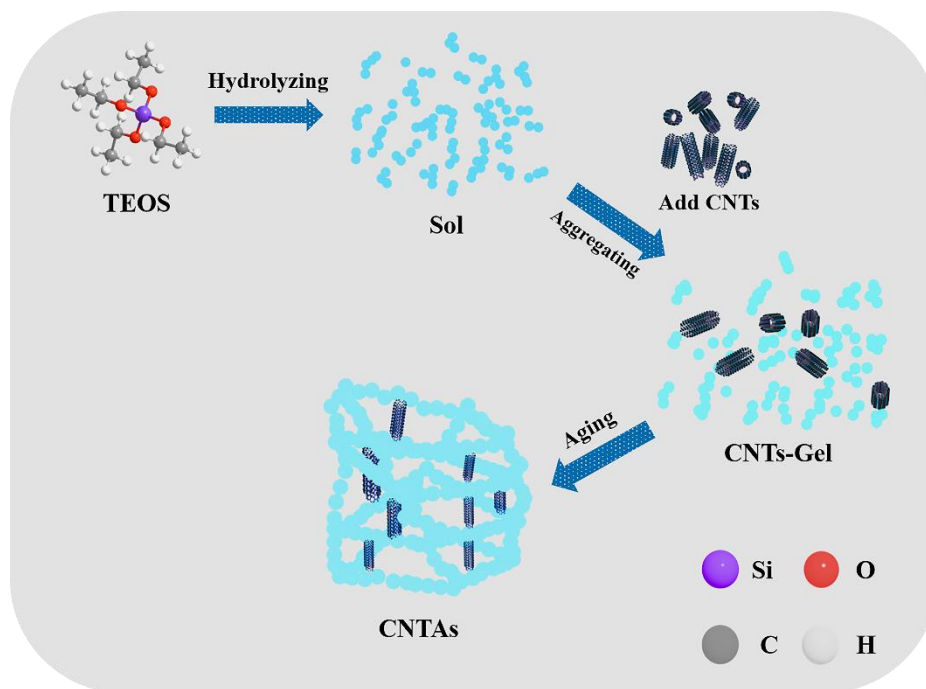
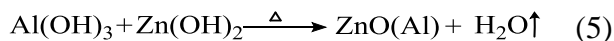
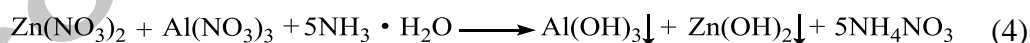


Fig. 2 The process of the preparation of carbon nanotube-doped aerogel (CNTAs).

### 2.3 Preparation of ZAO

The  $\text{Zn}(\text{NO}_3)_2$  solution and the  $\text{Al}(\text{NO}_3)_3$  solution were mixed and placed in a beaker, stirred and polyethylene glycol-1540 was added. Aqueous ammonia solution was added dropwise to the beaker to obtain a white precipitate, which was continuously added until the pH of the solution was 8 to 9. After dispersing, it was allowed to stand, and it was centrifuged and dried for 12 hours. Finally, calcined in a muffle furnace, the Al-doped ZnO (ZAO) powder is obtained. The ZAO was prepared as following reaction (4)-(5) [21, 22]:



### 2.4 Preparation of sandwich fabric-based composite material

The CNTAs obtained in step 2.3 is added to adhesive and the weight fraction of each component is: solvent (deionized water) is 60%, carbon nanotube aerogel is 15%, adhesive is 15 %, thickener is 5%, dispersant is 5%, mixing, stirring evenly, coated on PI fabric, hot pressed at 180 °C for 120 s, and obtained CNTAs/PI fabric.

The ZAO obtained in step 2.4 is added to adhesive, and the weight fraction of each component is: solvent (deionized water) is 70%, ZAO is 10%, adhesive is 10%,

and thickener is 5%, dispersing agent is 5%, mixing and stirring evenly, coated on CNTAs/PI fabric, drying and baking to obtain a sandwich fabric-based composite material (ZAO/CNTAs/PI fabric).

## 2.5 Characterizations

Scanning Electron Microscopy (SEM) was carried out on a TM-1000 scanning microscope (Hitachi, Japan) with a thin layer of gold film spraying on the surface of the samples to determine the morphology of samples at a microscale. The surface morphologies of the ZAO and CNTAs were observed by transmission electron microscopy (TEM, JEM-2100, Japan). The crystal structures of samples were recorded using X-ray diffraction (XRD, D/Max-2550, Japan) at room temperature with  $2\theta$  ranges from  $5^\circ$  to  $90^\circ$ , and were further confirmed by high-resolution TEM (JEM-2100, Japan). Thermogravimetric (TG) analysis was performed in 204 F1 analyzer (Netzsch, Germany) at the heating rate of  $20^\circ\text{C}/\text{min}$  and the temperature has ranged from  $25$  to  $880^\circ\text{C}$ . Thermal infrared imaging device (KREAVOR FLIR ONE3, FLIR Systems, Inc., USA) was utilized to test infrared radiation intensity of coating PI fabric. The samples were heated at  $60^\circ\text{C}$  for 20 seconds. (The infrared stealth properties of fabrics can be distinguished in a short time under high temperature.) The temperature differences on the surface of the samples were measured by a thermocouple thermometer. The limiting oxygen index (LOI) values of samples were measured according to an international standard ASTM D2863-2000 with FAA digital oxygen index apparatus (ATSFAAR, Italy). The thermal conductivity  $\text{W}/(\text{m}\cdot\text{K})$  of the PI fabric and CNTAs was measured using the DRL-III Thermal Conductivity Instrument. Ansys (Ansys, Inc. Canonsburg, Pennsylvania, USA) develops finite element analysis software for simulating engineering problems. In this paper, Ansys Workbench software is used for thermodynamic analysis. Typically, Ansys users break down larger structures into small components that are each modeled and tested separately. We start by defining the dimensions of the object and then increasing the thermal conductivity, temperature and other physical properties of the material. Finally, Ansys software simulates and analyzes the temperature distribution of the sample.

### 3 Results and discussion

#### 3.1 Morphology of PI fabric, ZAO and CNTAs

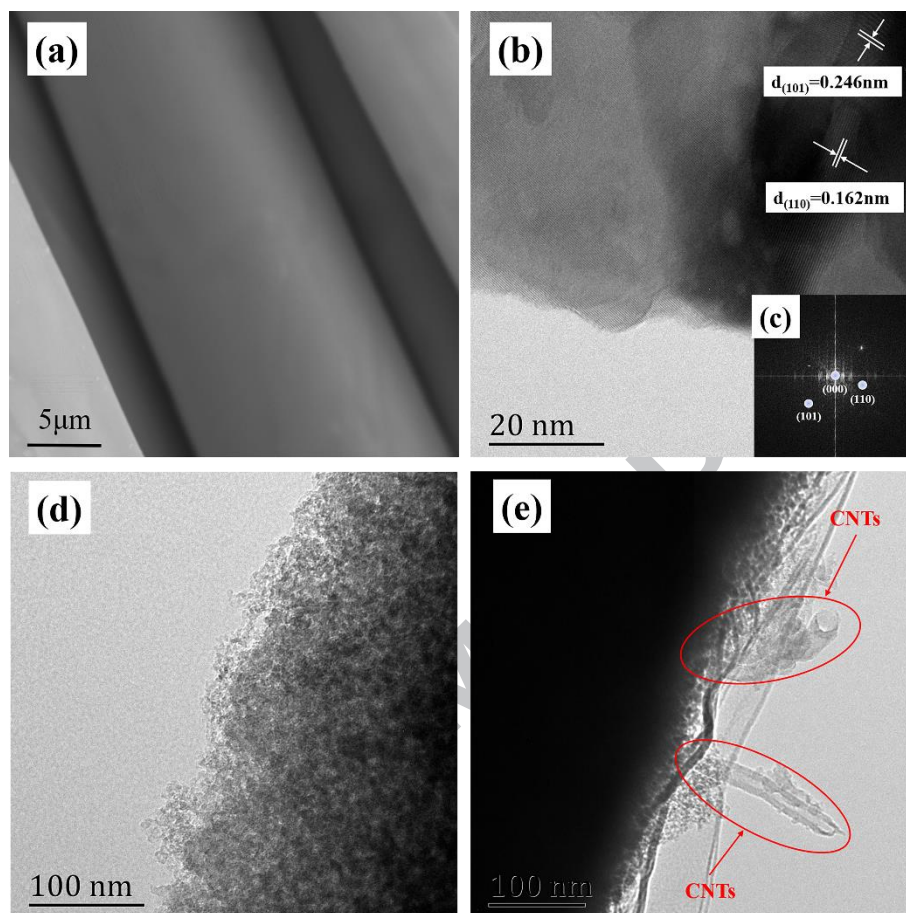


**Fig. 3** Morphology of PI fabric, ZAO and CNTAs: (a) SEM image of PI fabric; (b) high-resolution TEM (HRTEM) image of ZAO; (c) fast Fourier transform (FFT) image of ZAO; (d) and (e) TEM image of CNTAs.

The original PI fabric has a smooth surface and a cylindrical shape with a fiber diameter of 10-15  $\mu\text{m}$  from the scanning electron microscopy (SEM) images (Fig. 3(a)). Transmission electron microscopy (TEM) was performed to investigate the detailed structural features of the prepared ZAO and CNTAs, as shown in Fig. 3(b)-(e). The distinct lattice fringes of 0.246 nm and 0.162 nm in Fig. 3(b) correspond to the (101) planes and the (110) planes of ZAO, respectively. The TEM results are consistent with the crystal orientation observed by the XRD patterns. Fig. 3(c) is a fast Fourier transform (FFT) image, and the (101) and (110) planes are confirmed in the corresponding FFT image in Fig. 3(b). It can be seen from Fig. 3(d) that the CNTAs have a porous structure, leading to a high specific surface area. In the

Fig. 3(e), tubular CNTs can be seen embedded in the aerogel (marked with red circles in Fig. 3 (e)). Doping a small amount of CNTs can enhance the strength of the aerogels. When subjected to external forces, they are not easy to crush, and the thermal performance of the aerogel is not affected.

### 3.2 Thermogravimetric (TG) differential thermogravimetric (DTG) analysis

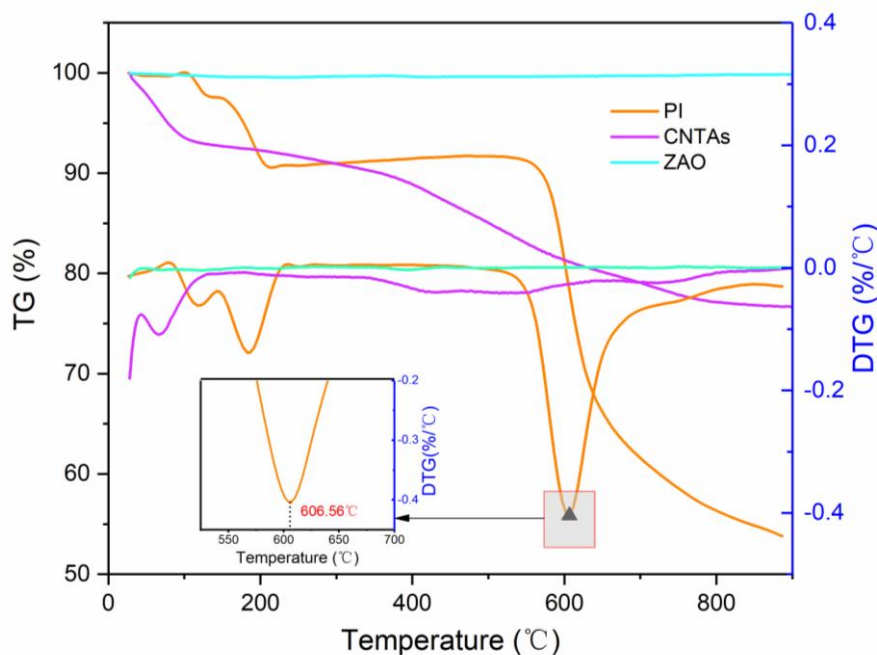


**Fig. 4** The thermogravimetric (TG) and differential thermogravimetric (DTG) analysis curves.

The thermal stability at different temperatures is an important parameter. Thermogravimetric (TG) and differential thermogravimetric (DTG) analysis are carried out in nitrogen to investigate thermal stability of PI, CNTAs and ZAO, as shown in Fig. 4. It can be seen from the Fig. 4 that there is almost no loss in the quality of the ZAO and the mass loss rate is almost zero from 0 °C to 900 °C. This indicates that the synthesized ZAO is very pure and does not decompose at high temperatures. It exhibits very good thermal stability and has very good high-temperature resistance. As can be seen from the Fig. 4, due to de-intercalation of water absorbed in the CNTAs, it displays a slight mass loss below 100 °C. The CNTAs exhibits a weight loss of about 16.8% at 100 °C-900 °C due to degradation of the -OH group and the CNTs, exhibiting excellent thermal stability up to 900 °C. Fig. 4 shows

the weight loss of PI against temperatures and the rate of weight loss as a function of temperature. As shown, PI left 53.8% char at 900 °C, these chars act as physical barrier and reduce the decomposition rate at higher temperatures.  $T_{10\%}$  and  $T_{max}$ , which are defined as the temperatures for the first 10% weight loss and the fastest weight loss, respectively.  $T_{10\%} = 206.56$  °C,  $T_{max} = 606.56$  °C, compared with ordinary fabrics such as PI and wool, PI fabrics have high decomposition temperature and strong thermal stability. Therefore, the sandwich fabric-based composite material prepared by ZAO, CNTAs, and PI with strong thermal stability and flame retardancy can successfully avoid combustion.

### 3.3 XRD analysis

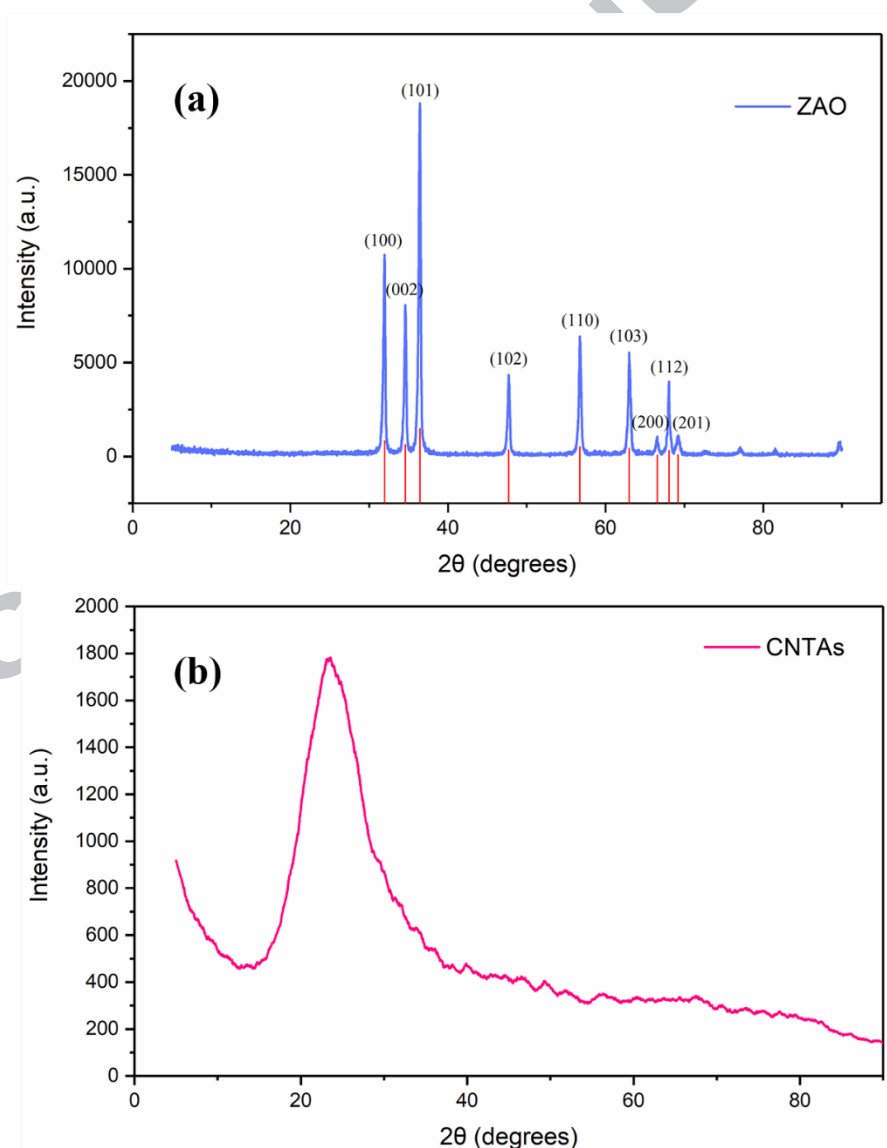


**Fig. 5** XRD patterns of (a) ZAO and (b) CNTAs.

The XRD spectrum of ZAO has no diffraction peak of  $\text{Al}_2\text{O}_3$  (Fig. 5(a)), which means that the Al element is not mixed in the ZnO crystal in a separate form, but replaces some Zn atoms in ZnO lattice by doping or occupies the voids in ZnO lattice [23]. Because the radius of the  $\text{Al}^{3+}$  ( $R_{\text{Al}} = 0.053 \text{ nm}$ ) is smaller than the radius of the  $\text{Zn}^{2+}$  ( $R_{\text{Zn}} = 0.072 \text{ nm}$ ), and the aluminum ion easily replaces the position of the zinc ion, forming oxygen vacancies and interstitial atoms and ZAO solid solution (Fig. 6).

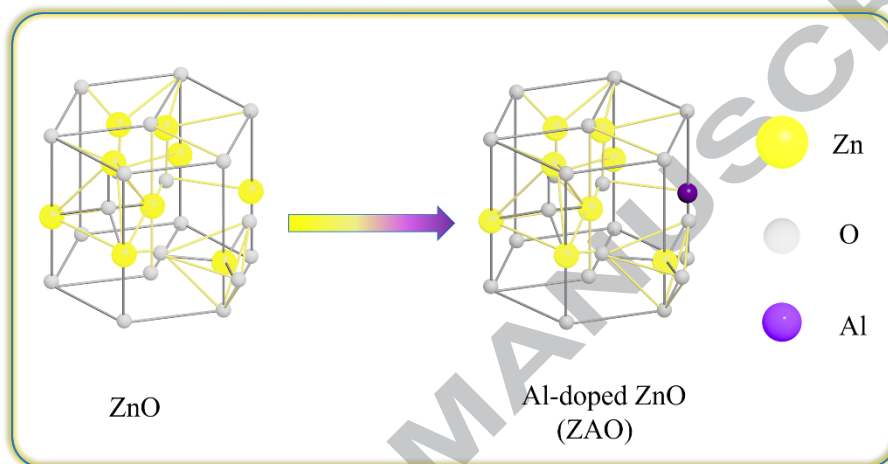


**Fig. 6** The crystalline structure changes from ZnO to ZAO.

It can be seen from the Fig. 5(a) that the position of the main peak is still consistent with the zinc oxide standard diffraction card JCPD36-1451, indicating that all products are ZnO, belonging to the hexagonal system [23-25], in the figure  $2\theta = 31.94^\circ, 34.60^\circ, 36.44^\circ, 47.70^\circ, 56.74^\circ, 63.00^\circ, 66.55^\circ, 68.03^\circ, 69.20^\circ$  corresponds to the (100), (002), (102), (101), (102), (110), (103), (200), (112), (201) diffraction planes of zinc oxide, and the diffraction peak shape is sharp and the diffraction intensity is high, demonstrating that the good crystallinity.

The Fig. 5(b) is an X-ray diffraction spectrum of a CNTAs sample. It can be seen from the figure that there is a diffuse diffraction peak in the range of  $2\theta = 0\sim 90^\circ$ , indicating that the CNTAs has a typical amorphous structure at room temperature, that is amorphous silica.

### 3.4 Thermodynamics analysis

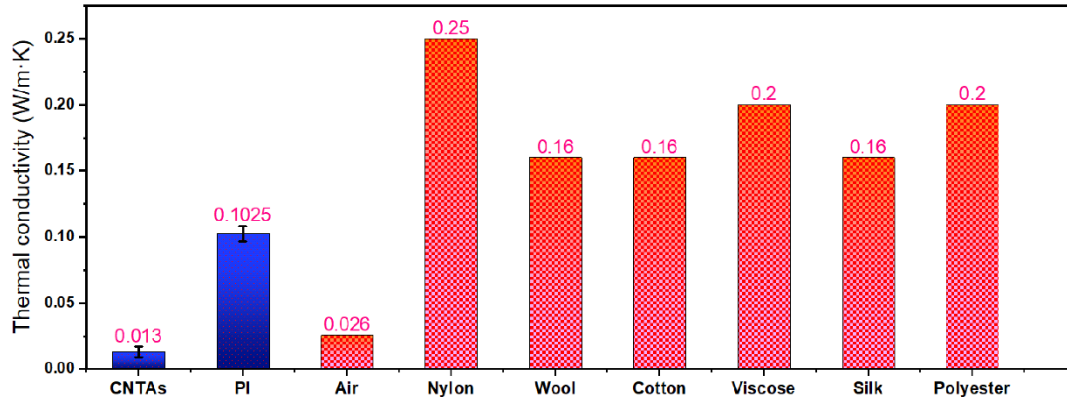


**Fig. 7** Thermal conductivity of CNTAs, PI fabric, air and common fabrics.

Compared with ordinary commercial fabrics [26], PI has the lowest thermal conductivity, so it has good thermal insulation properties. At room temperature and low relative humidity, the thermal conductivity of CNTAs was measured to be 0.13 W/(m·K) (Fig. 7), which is clearly lower than most commercial insulating thermal materials and air. Because its solids are composed of tiny three-dimensional network structures which connected to each other, the heat transfer through the solid phase will undergo complex tortuous passages, leading to good insulation effect. Similarly, since the mean free path of gas molecule motion is larger than the pore size of the aerogel, gas phase heat transfer is also greatly restricted. The total thermal conductivity of the CNTAs are: convective thermal conductivity, conducted thermal conductivity and thermal radiation. Thermal conductivity conduction contributions include gas conduction ( $\lambda_{gas}$ ) and solid conduction ( $\lambda_s$ ). Due to the low mass fraction and large surface area of aerogels, thermal radiation is also greatly limited. When the pore size of the material under normal pressure is smaller, the heat conduction caused by convection is negligible, so the heat conduction in the aerogel does not consider the influence of convective heat transfer. Due to the low temperature, the radiation contribution of CNTAs is negligible.

Solid phase conduction thermal conductivity[27, 28]:

$$\lambda_s = \rho \cdot v' \cdot \frac{\lambda_s'}{\rho_s \cdot v_s} \quad (6)$$

where  $\rho$  is the apparent density of CNTAs ( $\text{kg/m}^3$ ), measured value is  $3.0 \text{ kg/m}^3$ ;  $\rho_s$  is the skeletal density ( $\text{kg/m}^3$ ) =  $50\sim 150 \text{ kg/m}^3$ ;  $v'$  is the apparent density of CNAs

corresponding sound velocity (m/s);  $\nu_s$  is the CNAs skeleton density corresponding to the speed of sound (m/s);  $\lambda$  is the thermal conductivity of the base material (W/(m•K)), it is reported that the thermal conductivity of the base material is 1.34 W/(m•K) [27].

J. Fricke et al.[29, 30] give the relationship between aerogel thermal conductivity and density. The relationship between the aerogel solid phase thermal conductivity and its skeleton density is satisfied:

$$\lambda_s = C \cdot \rho_s^\alpha \quad (7)$$

where  $C$  is a constant and  $\alpha$  is an index,  $\approx 1.6$ .

The relationship between sound speed is [29, 30]:

$$v' \approx k' \left( \frac{\rho}{\rho_s} \right)^{0.88} \cdot \nu_s \quad (8)$$

In the above relationship, for the aerogel,  $k' = 0.39$ .

The tortuous complex solid-phase three-dimensional network structure can increase the heat transfer path in solid-phase heat conduction, which will result in low thermal conductivity. Granular aerogels have very low solid phase conduction due to the small amount of contact between the particles.

The CNTAs achieves its low thermal conductivity by utilizing the Knudsen effect without applying a vacuum in the pores. The gas thermal conductivity  $\lambda_{gas}$  considering the Knudsen effect can be written in a simplified way as [12, 31, 32]:

$$\lambda_{gas} = \frac{\lambda_{gas,0}}{1 + 2\beta \cdot Kn} = \frac{\lambda_{gas,0}}{1 + \sqrt{2}\beta \cdot k_b T / (\pi d^2 p \delta)} \quad (9)$$

where

$$Kn = \frac{\sigma_{mean}}{\delta} = \frac{k_b T}{\sqrt{2}\pi d^2 p \delta} \quad (10)$$

where  $\lambda_{gas}$  = gas thermal conductivity in the pores (W/(m•K)),  $\lambda_{gas,0}$  = gas thermal conductivity in the pores at standard temperature and pressure (W/(m•K)),  $\beta$  = coefficient characterizing the molecule-wall collision energy transfer efficiency (between 1.5 and 2.0),  $k_b$  = Boltzmann's constant  $\approx 1.38 \times 10^{-23}$  J/K,  $T$  = temperature (K),  $d$  = gas molecule collision diameter (m),  $p$  = gas pressure in pores (Pa),  $\delta$  =

characteristic pore diameter (m),  $\sigma_{mean}$  = mean free path of gas molecules (m).

According to the formula (6) and (9), the total thermal conductivity can be obtained the formula (11):

$$\lambda = \rho \cdot v' \cdot \frac{\lambda'_s}{\rho_s \cdot v_s} + \frac{\lambda_{gas,0}}{1 + \sqrt{2\beta \cdot k_b T / (\pi d^2 p \delta)}} \quad (11)$$

$$\text{Let } v' \approx k' \left( \frac{\rho}{\rho_s} \right)^{0.88} \cdot v_s \quad (12)$$

$$\lambda = 0.39 \lambda'_s \left( \frac{\rho}{\rho_s} \right)^{1.88} + \frac{\lambda_{gas,0}}{1 + \sqrt{2\beta \cdot k_b T / (\pi d^2 p \delta)}} \quad (13)$$

According to the above formula (13), the effective thermal conductivity is estimated to be 0.05037 W/(m•K) and the simplified model conforms to the actual measured value. However, there is still an error between the simulated value and the measured value due to changes in density, temperature and humidity.

### 3.5 Flame retardant properties

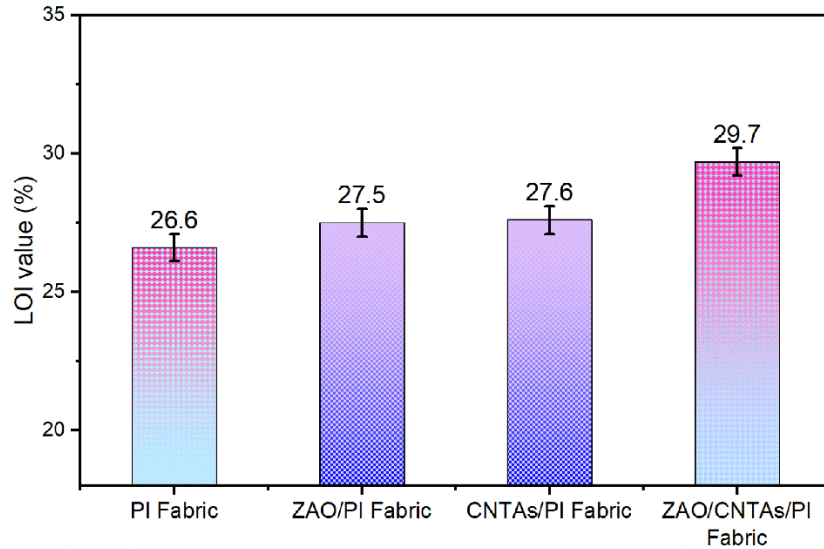


**Fig. 8** The LOI value of PI fabric, ZAO/PI fabric, CNTAs/PI fabric, and ZAO/CNTAs/PI fabric.

According to international standards (ASTM-D2863-2000), the limiting oxygen index (LOI) value refers to the volume fraction of oxygen in a mixed gas of oxygen and nitrogen that can maintain 1 cm of combustion. It is an index that characterizes the burning behavior of materials and is used to evaluate the flame retardancy of materials. The flame retardancy of the samples was evaluated by measuring the LOI values of PI fabric, ZAO/PI fabric, CNTAs/PI fabric, and ZAO/CNTAs/PI fabric,

sample size was 150 mm × 50 mm, and each set of samples was tested five times. Mostly, the higher the LOI value, the higher the flame retardancy of the substrate and the quantitative display of any change in the plasticity of the sample. As shown in the Fig. 8, the LOI values of PI fabric, ZAO/PI fabric, CNTAs/PI fabric, and ZAO/CNTAs/PI fabric were: 26.6%, 27.5%, 27.6%, 29.7%, respectively. The synergistic effect of ZAO and CNTAs effectively improve the flame retardant properties of PI fabric. This is may be due to the increased char yields as indicated by the TG results in Fig. 8. They can act as an effective barrier to heat, hindering the transfer of heat and fuel, and preventing the combustion. All in all, the material with this sandwich structure can successfully improve the flame retardancy of PI fabric.

### 3.6 Infrared stealth and thermal insulation simulation

Thermal analysis follows the first law of thermodynamics, the law of conservation of energy, for a closed system (no inflow or outflow of mass):

$$Q - W = \Delta U + \Delta KE + \Delta PE \quad (14)$$

Where:  $Q$  is heat;  $W$  is work;  $\Delta U$  is system internal energy;  $\Delta KE$  is system kinetic energy;  $\Delta PE$  is system potential energy;

For most engineering heat transfer problems:

$$\Delta KE = \Delta PE = 0 \quad (15)$$

Usually consider not doing work:  $W = 0$ , then:

$$Q = \Delta U \quad (16)$$

For steady-state thermal analysis:  $Q = \Delta U = 0$ , the heat that flows into the system is equal to the heat that flows out;

If the net heat flow rate of the system is zero, that is, the heat flowing into the system plus the heat generated by the system itself is equal to the heat flowing out of the system:

$$q_{inflow} + q_{generation} - q_{out} = 0 \quad (17)$$

the system is in a hot steady state. The temperature of any node in the steady state thermal analysis does not change with time. The energy balance

equation for steady-state thermal analysis is (in matrix form):

$$[K]\{T\} = \{Q\} \quad (18)$$

where  $[K]$  is the conduction matrix, including thermal conductivity, convection coefficient and radiance and shape factor;  $\{T\}$  is the node temperature vector;  $\{Q\}$  is the node heat flow rate vector, including heat generation; ANSYS uses model geometric parameters, material thermal performance parameters and applied boundaries conditions to generate  $[K]$ ,  $\{T\}$  and  $\{Q\}$ .

According to the structural characteristics of the sandwich fabric-based composite material, the geometric model of the multi-layer fabric system was established, and the thermal conductivity of the multilayer fabric system was numerically simulated by selecting the steady-state heat conduction calculation model.

According to the law of conservation of energy, the energy equation between multilayer fabrics is as follows:

$$(\rho c_p) \frac{\partial T}{\partial t} = \frac{\partial}{\partial x} \left( \lambda T \frac{\partial T}{\partial x} \right) + \frac{\partial q}{\partial x} \quad (19)$$

where  $\rho$  is the density of the fabric ( $\text{kg}/\text{m}^3$ );  $c_p$  is the specific heat capacity of the fabric ( $\text{J}/(\text{kg}\cdot\text{K})$ );  $\lambda$  is the thermal conductivity of the fabric ( $\text{W}/(\text{m}\cdot\text{K})$ );  $t$  is the time (s);  $x$  is the position of any point of the fabric in the x-axis direction;  $q$  is the heat absorbed by the fabric ( $\text{W}/\text{m}^2$ ).

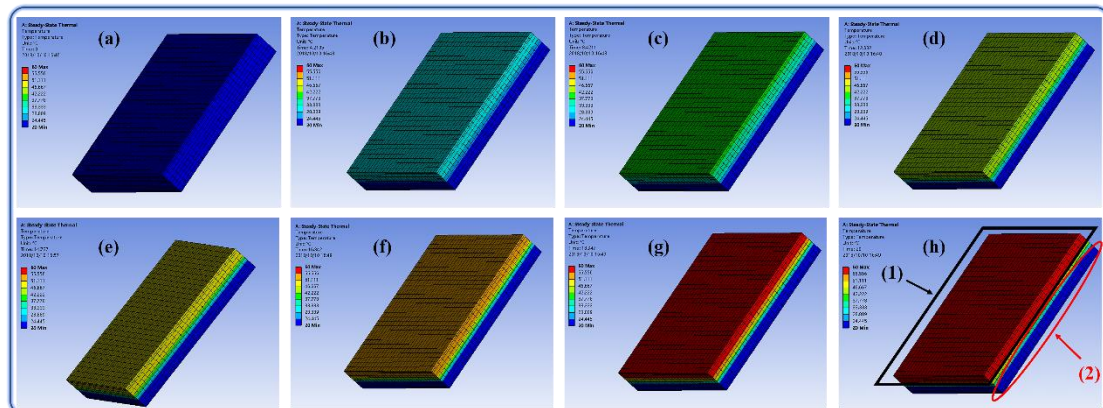


**Fig. 9** ANSYS Workbench software simulates the temperature distribution of the sandwich fabric-based composite material after heating 60 °C for 20 s.

The steps are as follows: (1) Steady-state thermal (ANSYS); (2) Setting the thermal performance parameters of various materials in the Engineering Data project, mainly the thermal conductivity, density and specific heat capacity of the material; (3) Establish geometric modeling of multi-layer fabrics in the Geometry project; (4) Enter the Mechanical analysis environment in the Setup project to define the corresponding materials for the geometric model established in the Geometry module; (5) Meshing in the Mesh module. (6) Applying a boundary condition to apply a temperature load on one side of the sandwich fabric-based composite material; (7) Set the required solution results, including the overall temperature field distribution cloud map of the multi-layer fabric, and the overall heat flux density distribution cloud map; (8) Save the solution result, perform post-processing, and so on [33].

The simulation results are shown in the Fig. 9((a)-(h)), and the overall temperature field distribution of the sandwich fabric-based composite material in 20s is captured. The Fig. 9 shows that the thermal conductivity is very slow due to the influence of the insulation. When a temperature load is applied on one side, the temperature on the other side has little effect (marked with black and red circles in Fig. 9 (h): (1) and (2) respectively).

The radiation intensity of the target is proportional to the radiation flux density of the target. According to the Tiffin-Boltzmann law, the radiation capacity of the target depends on the temperature of the target and the emissivity of the target. ZAO with low emissivity can reduce the surface emissivity of sandwich fabric-based composite material to 0.5. For imaging detection, which mainly detects the background and the thermal radiation energy emitted by the target, and compares the difference between the two radiant energy to identify the target. The contrast of the recognition is as follows [34]:

$$\Delta G = \frac{E_0 - E_B}{E_B} \quad (20)$$

where  $\Delta G$  is the contrast,  $E_0$  is the target radiant energy density,  $E_B$  background

radiant energy density.

The maximum distance  $R_{max}$  that the infrared detection system can detect is:

$$R_{max} = \sqrt{\frac{J \cdot \tau_a \cdot \pi \cdot V_n}{2(NA) \cdot D^* \cdot V_s \cdot \sqrt{\omega \cdot \Delta f}}} \quad (21)$$

where  $J$  is the target radiation intensity;  $\tau_a$  is the atmospheric transmittance;  $NA$  is the numerical aperture of the optical system;  $D^*$  is the detector's detection rate;  $\omega$  is the instantaneous field of view;  $\Delta f$  is the system bandwidth;  $V_n$  is the noise level;  $V_s$  is the signal level.

It can be seen from the formula (21) that one of the main purposes of infrared stealth is to reduce the infrared radiation characteristic ( $J$ ) of the target, so that its detectable distance can be reduced. The radiation intensity of the target is proportional to the radiation emission of the target.

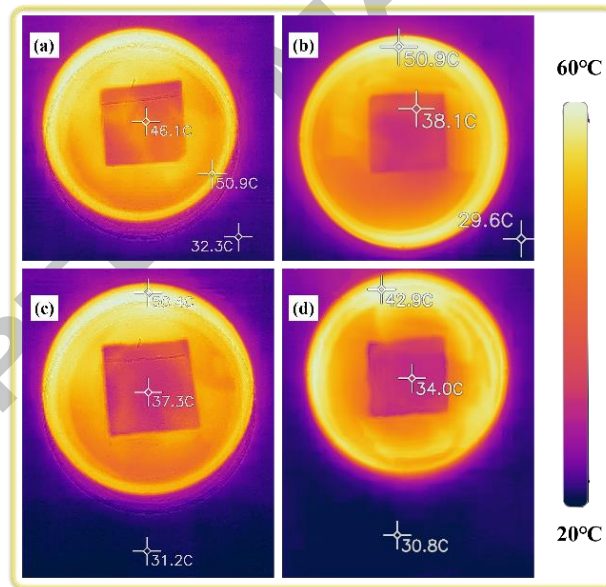


**Fig.10** The IR thermal images of (a) PI fabric, (b) ZAO/PI fabric, (c) CNTAs/PI fabric, and (d) ZAO/CNTAs/PI fabric.

IR thermal images of PI fabric, ZAO/PI fabric, CNTAs/PI fabric, and ZAO/CNTAs/PI fabric heated under a heat source by an infrared thermal imager. As shown in the Fig. 10((a)-(c)), the PI fabric has a large infrared radiation intensity under the heat source, while the ZAO/PI fabric and CNTAs/PI fabric are slowly raised under heating. However, the infrared radiation intensity of ZAO/CNTAs/PI fabric is very small and the temperature difference with the environment is also subtle when

heated under the heat source (Fig. 10(d)). Therefore, the sandwich fabric-based composite material produced in this paper can effectively lower the target radiation intensity and reduces the probability of being detected by the infrared detector.

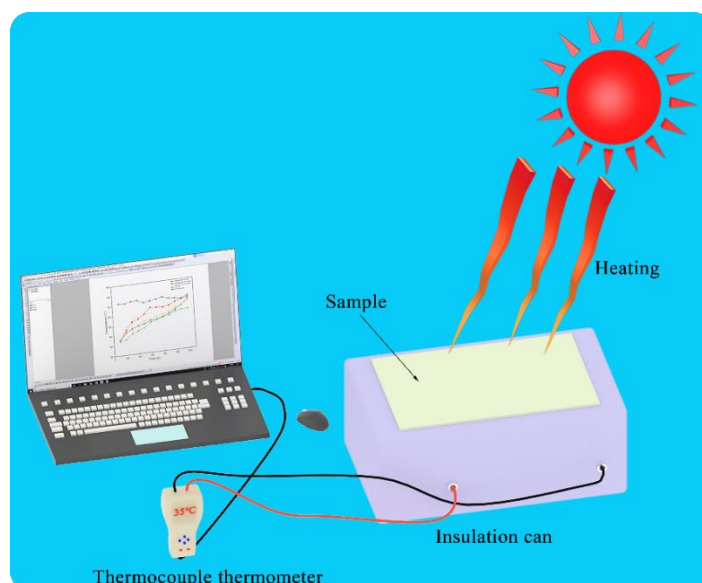


**Fig. 11** A simple device for testing the temperature change of samples under sunlight.

In order to test the temperature change of the samples under direct sunlight, the samples were heated to 30 °C. As shown in the Fig. 11, the self-made open insulation-can places the sample in the opening and is exposed to the direct sunlight. (The outdoor humidity is 37%, located in Shanghai, China, the weather is clear.) Test the temperature rise of the samples in direct sunlight for 120 s. As shown in the Fig. 12, the environment temperature is  $42 \pm 1$  °C, a very high outdoor temperature. The PI fabric heating rate is very fast and rises to 41 °C within 60 s. The heating rate of PI ZAO/PI fabric and CNTAs/PI fabric are slower. While the heating rate of the sandwich fabric base composites was significantly slowly raised and the surface temperature was 41 °C after 120 s. This indicates that the as-prepared ZAO/CNTAs/PI fabric has obvious heat insulation effect, and making it a good candidate in outdoor infrared stealth and thermal protection fields.

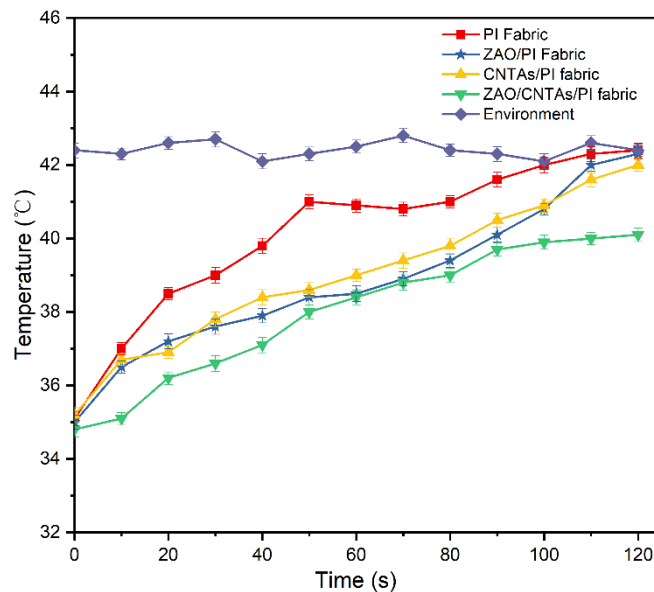


**Fig. 12** The temperature change curves of the samples under direct sunlight in 120s.

## 4 Conclusions

At present, infrared stealth materials for advanced detection and stealth technology are important in many fields. A CNTs-doped aerogel was firstly hot pressed on the surface of PI fabric, and then coated low-emissivity ZAO on the outer surface. The surface emissivity of the resultant composite is less than 0.5, and the thermal conductivity of the intermediate layer aerogel is as low as 0.013 W/(m·K). Through experiments, theoretical derivation and simulation, the results demonstrated that it had high-performance infrared stealth and super insulation effect. Therefore, the as-prepared functional material based on PI fabric can be used as a potential military textile material for infrared camouflage outfits and thermal protection for people working under high temperature and so on.

## Acknowledgements

The research was supported by National Science Foundation of China (NSFC) (No. 51403032).

## References

- [1] Mao Z, Wang W, Liu Y, Zhang L, Xu H, Zhong Y. Infrared stealth property based on semiconductor (M)-to-metallic (R) phase transition characteristics of W-doped VO<sub>2</sub> thin films coated on cotton fabrics. *Thin Solid Films*. 2014;558:208-14.
- [2] Zhang C, Yang J, Yuan W, Zhao J, Dai JY, Guo TC, et al. An ultralight and thin metasurface for radar-infrared bi-stealth applications. *Journal of Physics D: Applied Physics*. 2017;50:444002.
- [3] Cui Y, Gong H, Wang Y, Li D, Bai H. A Thermally Insulating Textile Inspired by Polar Bear Hair. *Adv Mater*. 2018;30:e1706807.
- [4] Liu X-F, Lai Y-K, Huang J-Y, Al-Deyab SS, Zhang K-Q. Hierarchical SiO<sub>2</sub>@Bi<sub>2</sub>O<sub>3</sub> core/shell electrospun fibers for infrared stealth camouflage. *Journal of Materials Chemistry C*. 2015;3:345-51.
- [5] Yu H, Xu G, Shen X, Yan X, Cheng C. Low infrared emissivity of polyurethane/Cu composite coatings. *Applied Surface Science*. 2009;255:6077-81.
- [6] Wu K-H, Cheng K-F, Wang J-C, Chang Y-C. Preparation of magnetic expanded graphite with microwave absorption and infrared stealth characteristics. *Materials Express*. 2017;7:500-8.
- [7] Andersson SK, Staaf O, Olsson PO, Malmport A, Ribbing CG. Infrared properties of beta-sialon as a function of composition. *Optical Materials*. 1998;10:85-93.
- [8] Yu ZL, Yang N, Apostolopoulou-Kalkavoura V, Qin B, Ma ZY, Xing WY, et al. Fire-Retardant and Thermally Insulating Phenolic-Silica Aerogels. *Angew Chem Int Ed Engl*. 2018;57:4538-42.
- [9] Al-Homoud DMS. Performance characteristics and practical applications of common building thermal insulation materials. *Building and Environment*. 2005;40:353-66.
- [10] Apostolopoulou-Kalkavoura V, Gordeyeva K, Lavoine N, Bergström L. Thermal conductivity of hygroscopic foams based on cellulose nanofibrils and a nonionic polyoxamer. *Cellulose*. 2017;25:1117-26.
- [11] Li T, Song JW, Zhao XP, Yang Z, Pastel G, Xu SM, et al. Anisotropic, lightweight, strong, and super thermally insulating nanowood with naturally aligned nanocellulose. *Science Advances*. 2018;4:9.
- [12] Jelle BP. Traditional, state-of-the-art and future thermal building insulation materials and solutions – Properties, requirements and possibilities. *Energy and Buildings*. 2011;43:2549-63.
- [13] Krstulović N, Salamon K, Budimlija O, Kovač J, Dasović J, Umek P, et al. Parameters optimization for synthesis of Al-doped ZnO nanoparticles by laser ablation in water. *Applied Surface Science*. 2018;440:916-25.
- [14] Hussain SQ, Le AHT, Mallem K, Park H, Ju M, Kim Y, et al. Using the light scattering properties of multi-textured AZO films on inverted hemisphere textured glass surface morphologies to improve the efficiency of silicon thin film solar cells. *Applied Surface Science*. 2018;447:866-75.
- [15] Gong L, Ye Z, Lu J, Zhu L, Huang J, Gu X, et al. Highly transparent conductive and near-infrared reflective ZnO:Al thin films. *Vacuum*. 2010;84:947-52.
- [16] Ahmad F, Ulker Z, Erkey C. A novel composite of alginate aerogel with PET nonwoven with enhanced thermal resistance. *Journal of Non-Crystalline Solids*. 2018;491:7-13.
- [17] Kim C-Y, Lee J-K, Kim B-I. Synthesis and pore analysis of aerogel-glass fiber composites by ambient drying method. *Colloids and Surfaces A: Physicochemical and Engineering Aspects*. 2008;313-314:179-82.
- [18] Kang K, Lee KH, Han Y, Gao H, Xie S, Muller DA, et al. Layer-by-layer assembly of two-dimensional materials into wafer-scale heterostructures. *Nature*. 2017;550:229-33.

- [19] Wu X, Lyu J, Hong G, Liu XC, Zhang X. Inner Surface-Functionalized Graphene Aerogel Microgranules with Static Microwave Attenuation and Dynamic Infrared Shielding. *Langmuir*. 2018;34:9004-14.
- [20] Wang D, Yu H, Fan X, Gu J, Ye S, Yao J, et al. High Aspect Ratio Carboxylated Cellulose Nanofibers Cross-linked to Robust Aerogels for Superabsorption-Flocculants: Paving Way from Nanoscale to Macroscale. *ACS Appl Mater Interfaces*. 2018;10:20755-66.
- [21] Lv Y, Zhang Z, Yan J, Zhao W, Zhai C. Al doping influences on fabricating ZnO nanowire arrays: Enhanced field emission property. *Ceramics International*. 2018;44:7454-60.
- [22] Cao F, Li C, Li M, Li H, Huang X, Yang B. Direct growth of Al-doped ZnO ultrathin nanosheets on electrode for ethanol gas sensor application. *Applied Surface Science*. 2018;447:173-81.
- [23] Maki H, Ichinose N, Ohashi N, Haneda H, Tanaka J. Lattice relaxation of a ZnO(0001) surface accompanied by a decrease in antibonding feature. *Journal of Crystal Growth*. 2001;229:114-8.
- [24] Gordon RG. Criteria for Choosing Transparent Conductors. *MRS Bulletin*. 2011;25:52-7.
- [25] Haug FJ, Geller Z, Zogg H, Tiwari AN, Vignali C. Influence of deposition conditions on the thermal stability of ZnO:Al films grown by rf magnetron sputtering. *Journal of Vacuum Science & Technology A: Vacuum, Surfaces, and Films*. 2001;19:171-4.
- [26] Jelle BP. Traditional, state-of-the-art and future thermal building insulation materials and solutions - Properties, requirements and possibilities. *Energy and Buildings*. 2011;43:2549-63.
- [27] Hrubesh LW, Pekala RW. Thermal properties of organic and inorganic aerogels. *Journal of Materials Research*. 1994;9:731-8.
- [28] Lee OJ, Lee KH, Yim TJ, Kim SY, Yoo KP. Determination of mesopore size of aerogels from thermal conductivity measurements. *Journal of Non-Crystalline Solids*. 2002;298:287-92.
- [29] Heinemann U, Caps R, Fricke J. Radiation conduction interaction: An investigation on silica aerogels. *International Journal of Heat and Mass Transfer*. 1996;39:2115-30.
- [30] Fricke J, Tillotson T. Aerogels: production, characterization, and applications. *Thin Solid Films*. 1997;297:212-23.
- [31] Baetens R, Jelle BP, Thue JV, Tenpierik MJ, Grynning S, Uvsløkk S, et al. Vacuum insulation panels for building applications: A review and beyond. *Energy and Buildings*. 2010;42:147-72.
- [32] Jelle BP, Gustavsen A, Baetens R. The path to the high performance thermal building insulation materials and solutions of tomorrow. *Journal of Building Physics*. 2010;34:99-123.
- [33] Bai JB, Shenoi RA, Xiong JJ. Thermal analysis of thin-walled deployable composite boom in simulated space environment. *Composite Structures*. 2017;173:210-8.
- [34] Zhang Z, Xu M, Ruan X, Yan J, Yun J, Zhao W, et al. Enhanced radar and infrared compatible stealth properties in hierarchical SnO<sub>2</sub>@ZnO nanostructures. *Ceramics International*. 2017;43:3443-7.

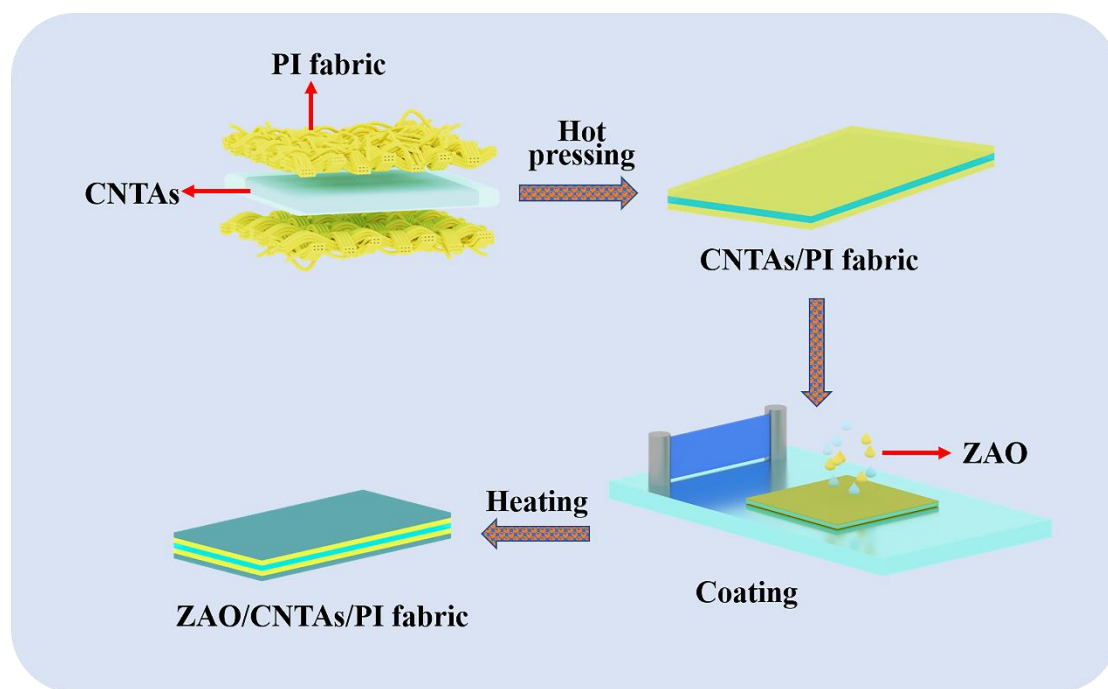


**Fig. 1** The process of the preparation of multilayer sandwich fabric-based composite material (ZAO/CNTAs/PI fabric).

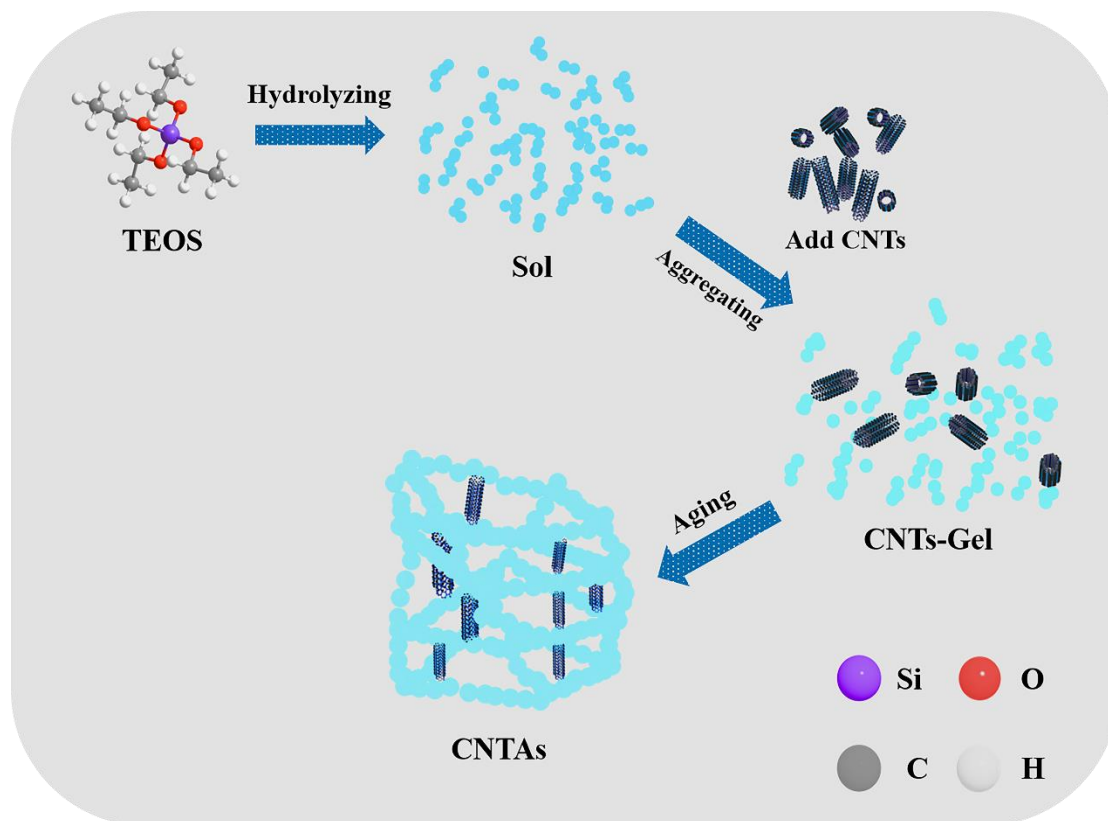


**Fig. 2** The process of the preparation of carbon nanotube-doped aerogel (CNTAs).

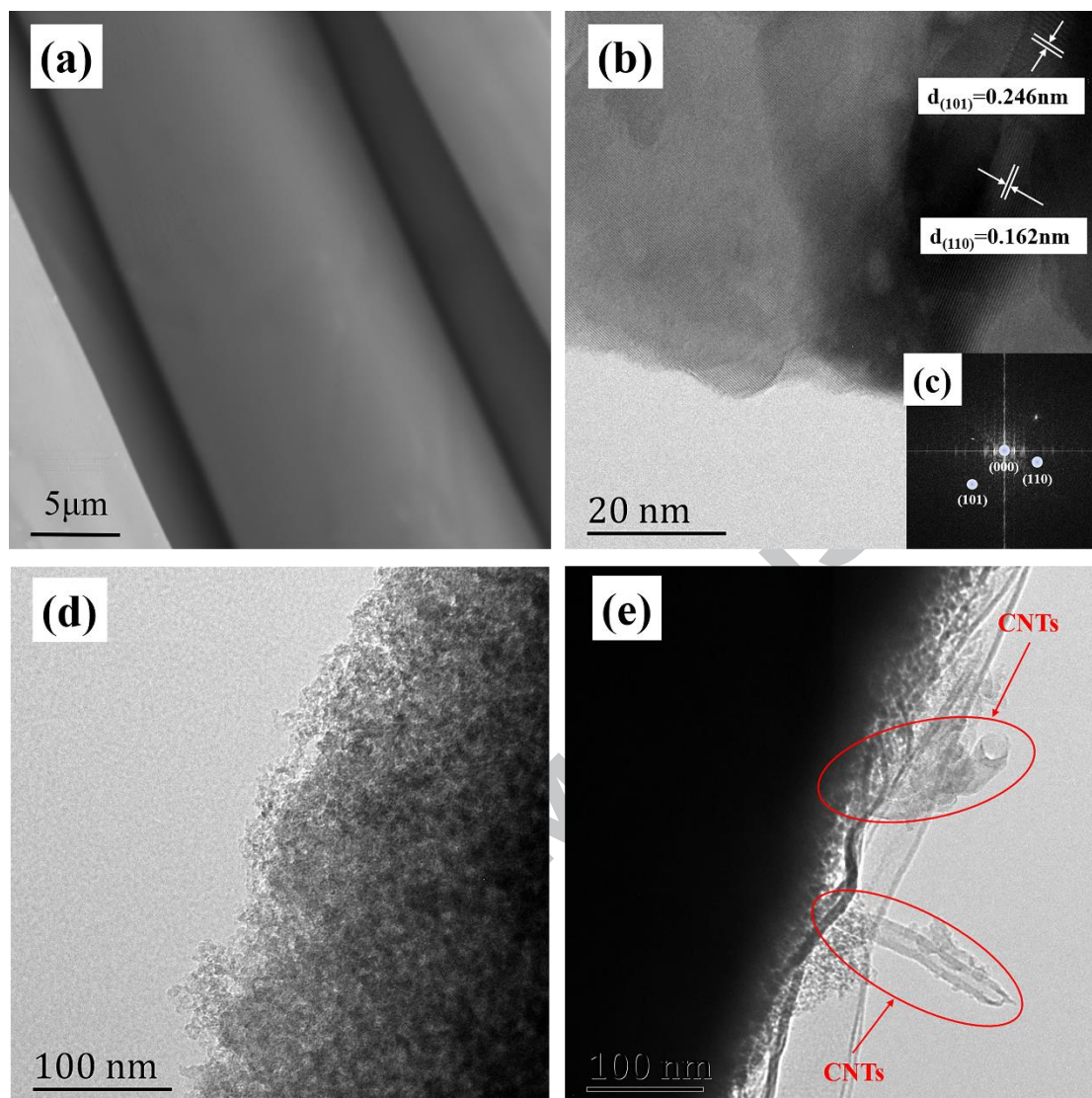


**Fig. 3** Morphology of PI fabric, ZAO and CNTAs: (a) SEM image of PI fabric; (b) high-resolution TEM (HRTEM) image of ZAO; (c) fast Fourier transform (FFT) image of ZAO; (d) and (e) TEM image of CNTAs.

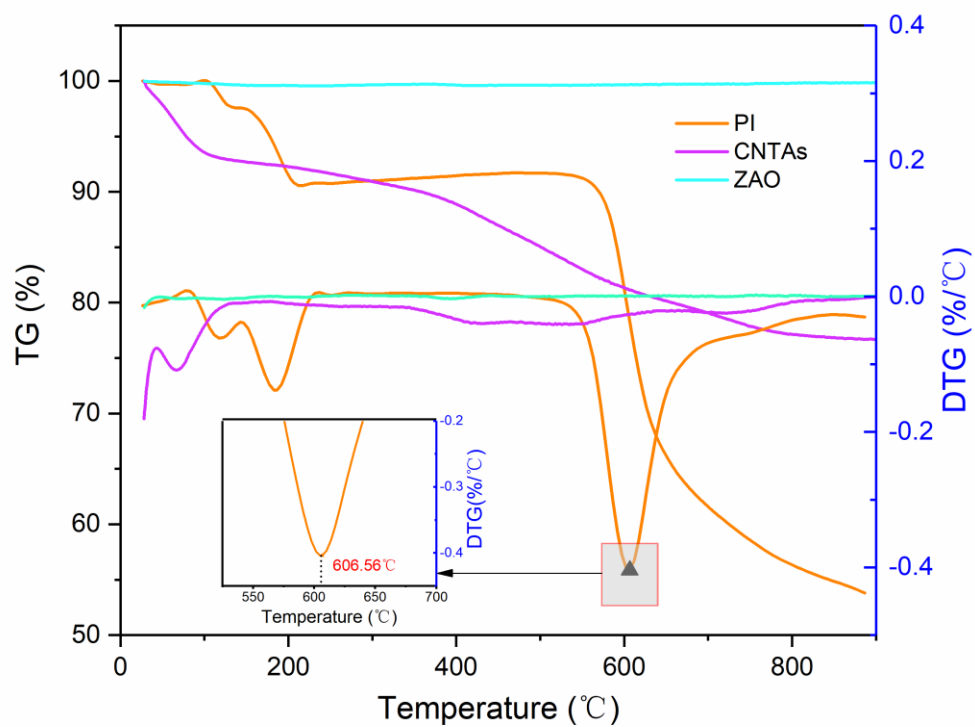


**Fig. 4** The thermogravimetric (TG) and differential thermogravimetric (DTG) analysis curves.

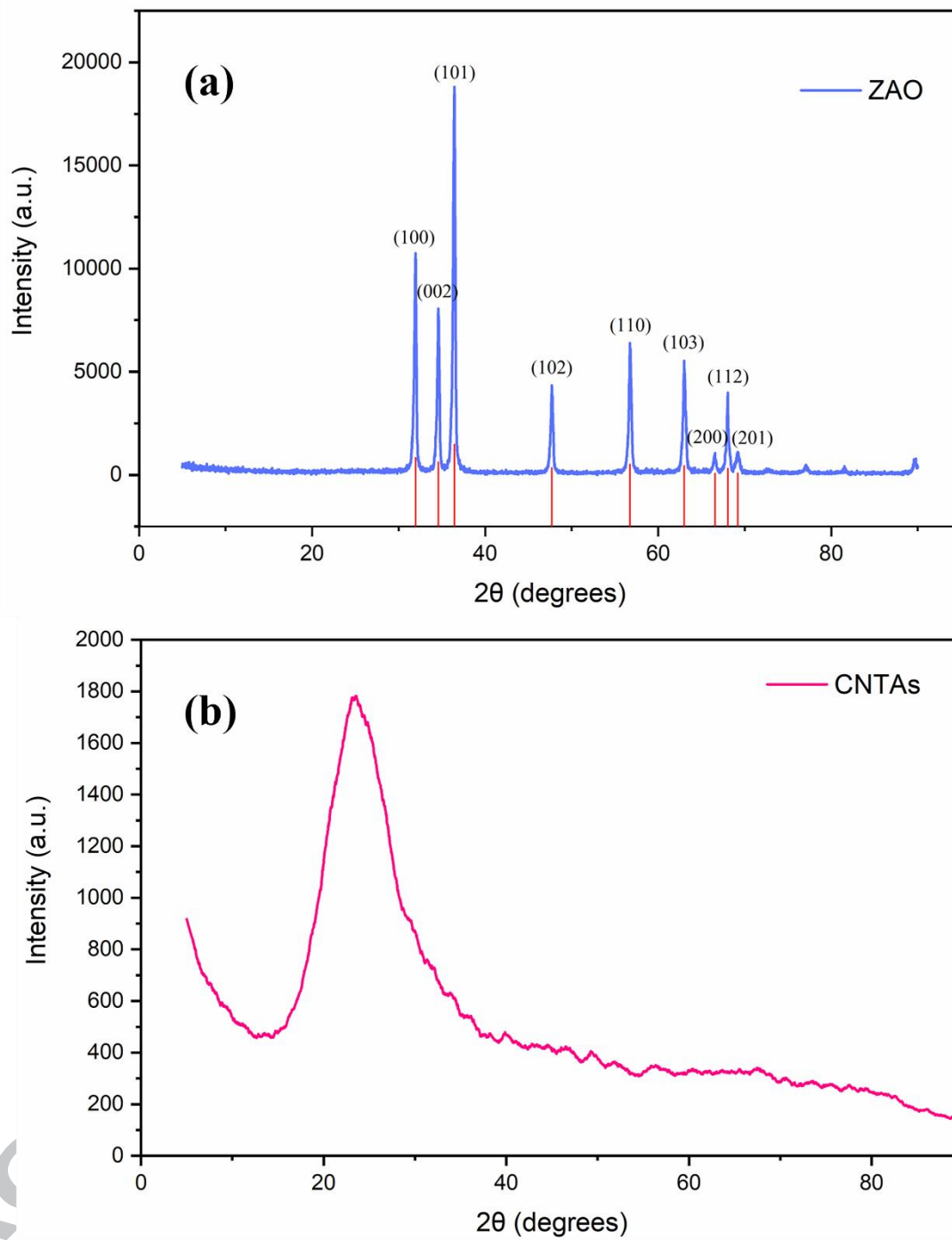
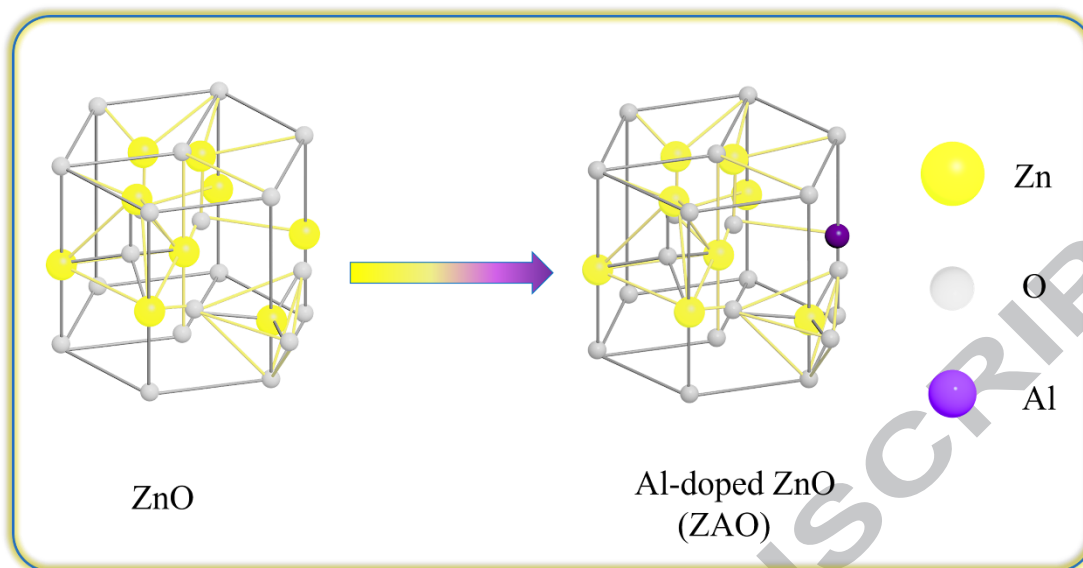
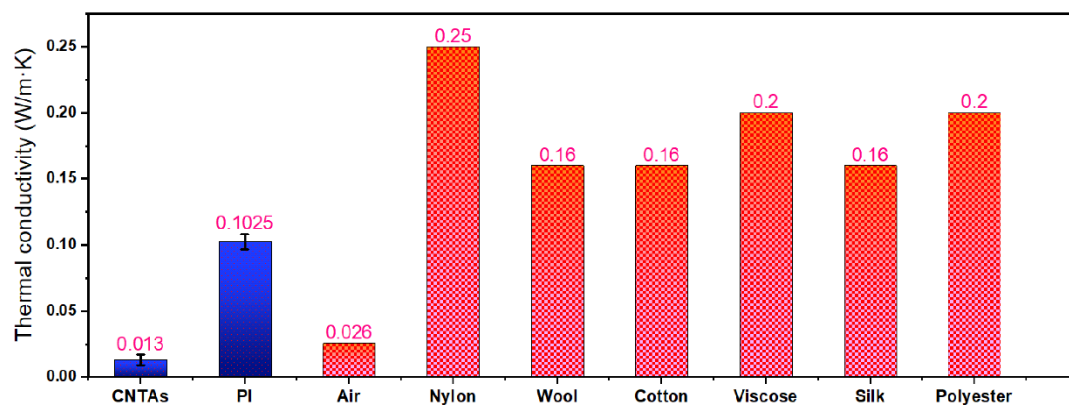


Fig. 5 XRD patterns of (a) ZAO and (b) CNTAs.



**Fig. 6** The crystalline structure changes from ZnO to ZAO.



**Fig. 7** Thermal conductivity of CNTAs, PI fabric, air and common fabrics.

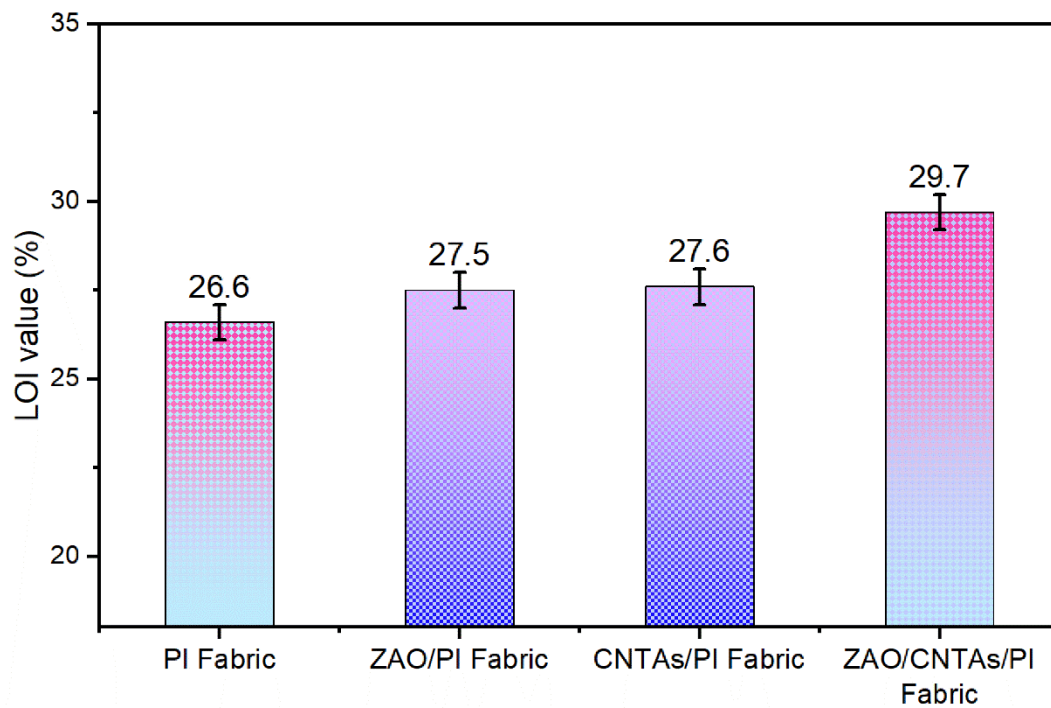


**Fig. 8** The LOI value of PI fabric, ZAO/PI fabric, CNTAs/PI fabric, and ZAO/CNTAs/PI fabric.

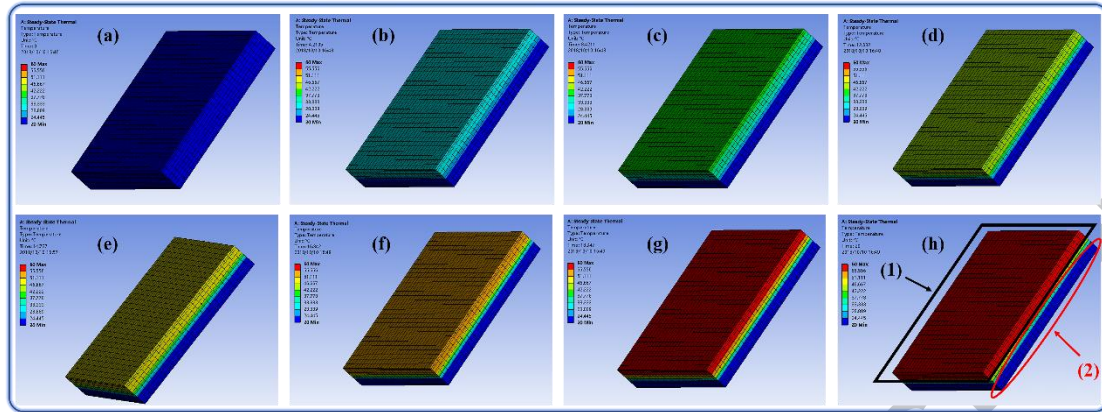


**Fig. 9** ANSYS Workbench software simulates the temperature distribution of the sandwich fabric-based composite material after heating 60 °C for 20 s.

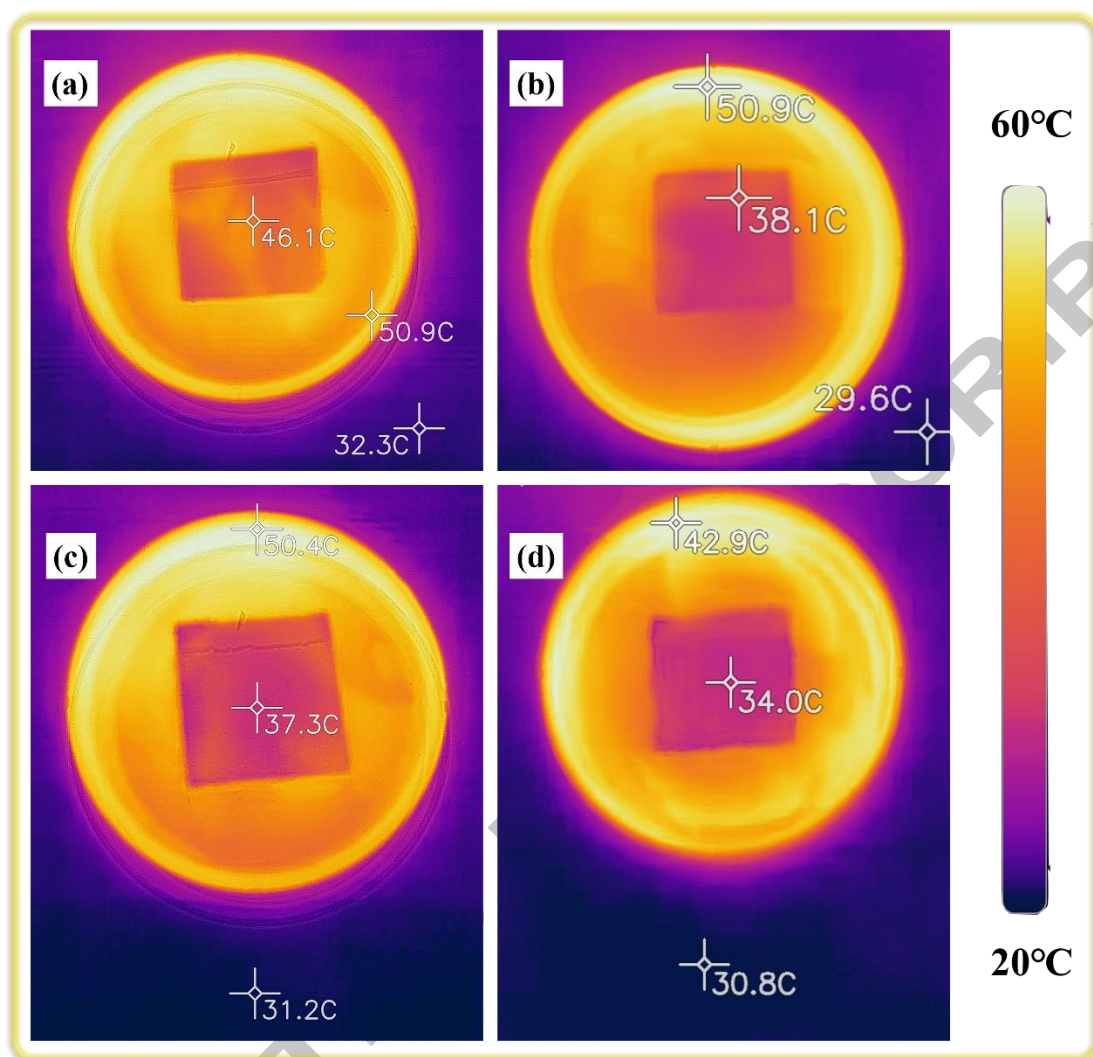


**Fig.10** The IR thermal images of (a) PI fabric, (b) ZAO/PI fabric, (c) CNTAs/PI fabric, and (d) ZAO/CNTAs/PI fabric.

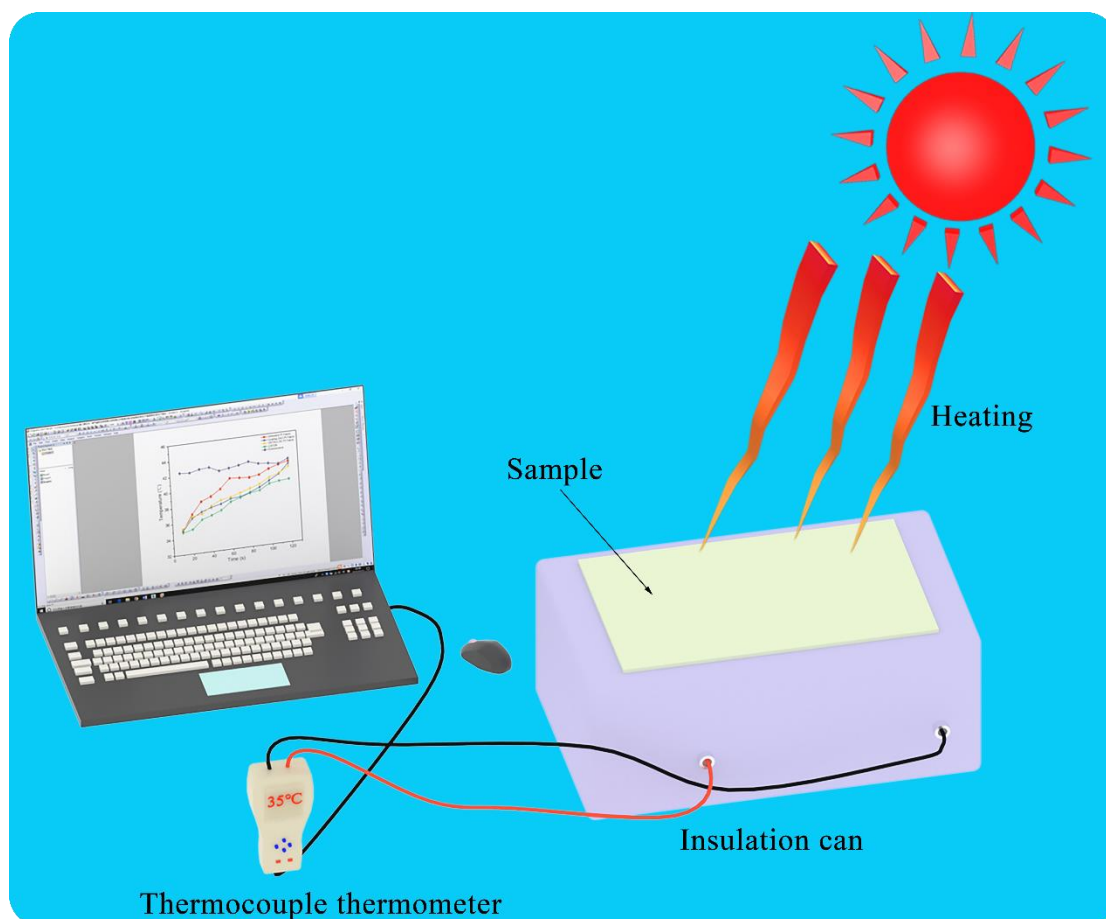


**Fig. 11** A simple device for testing the temperature change of samples under sunlight.

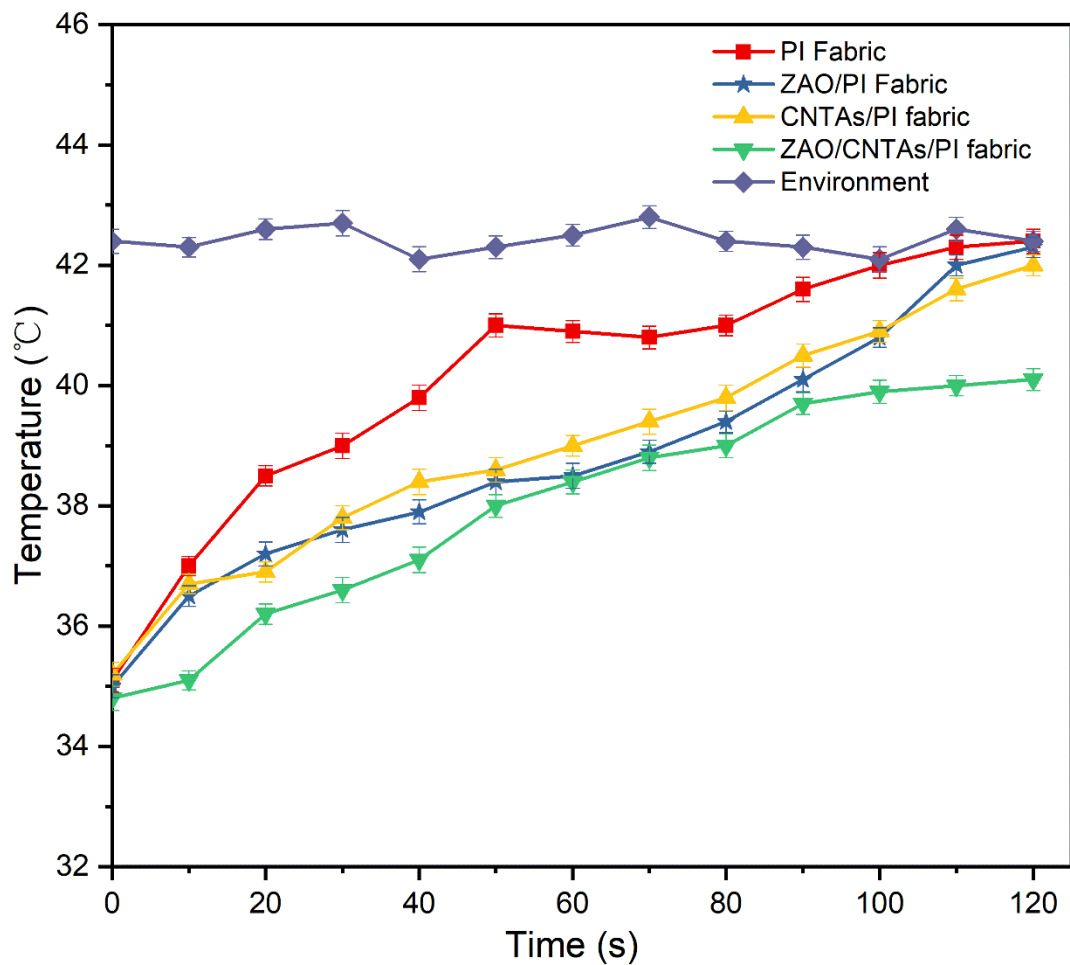


Fig. 12 The temperature change curves of the samples under direct sunlight in 120s.